DOI: 10.1002/((please add manuscript number))
Article type: Communication

In-situ Observation of Low-Power Nano-Synaptic Response in Graphene Oxide using Conductive Atomic Force Microscopy

Fei Hui, Peisong Liu, Stephen A. Hodge, Tian Carey, Chao Wen, Felice Torrisi, D. Thanuja L. Galhena, Flavia Tomarchio, Yue Lin, Enrique Moreno, Juan B. Roldan, Elad Koren, Andrea C. Ferrari, Mario Lanza**

Dr. F. Hui, Prof. E. Koren
Department of Materials Science and Engineering, Technion - Israel Institute of Technology, Haifa 3200003, Israel.
E-mail: fei.hui@campus.technion.ac.il

Dr. P. Liu, C. Wen,
Institute of Functional Nano & Soft Materials, Collaborative Innovation Center of Suzhou Nanoscience and Technology, Soochow University, 199 Ren-Ai Road, Suzhou 215123, China.

Dr. S. A. Hodge, Dr, D. T. L. Galhena, F. Tomarchio, D. Y. Lin, Prof. A. C. Ferrari
Cambridge Graphene Centre, University of Cambridge, 9 JJ Thomson Avenue, Cambridge, CB3 0FA, UK

Dr. T. Carey, Prof. F. Torrisi,
Department of Chemistry, Molecular Sciences Research Hub, Imperial College London, White City Campus, Wood Lane, London W12 0BZ, UK

Dr. E. Moreno, Prof. J. B. Roldan
Departamento de Electrónica y Tecnología de Computadores, Universidad de Granada, Facultad de Ciencias, Avd. Fuentenueva s/n, 18071 Granada, Spain

Prof. M. Lanza
Physical Science and Engineering Division, King Abdullah University of Science and Technology (KAUST), Thuwal 23955-6900, Saudi Arabia
E-mail: mario.lanza@kaust.edu.sa

Abstract

Multiple studies have reported the observation of electro-synaptic response in different metal/insulator/metal devices; however, most of them analysed large (>1 μm^2) devices that do not meet the integration density required by the industry (10^{10} devices/mm^2). Some studies

employed a scanning tunnelling microscope (STM) to explore nano-synaptic response in different materials, but in this setup there is a nanogap between the insulator and one of the metallic electrodes (i.e. the STM tip), which is not present in real devices. Here we show how to use a conductive atomic force microscope (CAFM) to explore the presence and quality of nano-synaptic response in confined areas <500 nm^2. For this study, we selected graphene oxide (GO) due to its easy fabrication and excellent electrical properties. Our experiments indicate that metal/GO/metal nano-synapses exhibit potentiation and paired pulse facilitation with low write current levels <1 μA (i.e. power consumption ~3 μW), controllable excitatory post-synaptic currents and long-term potentiation and depression. Our results provide a new method to explore nano-synaptic plasticity at the nanoscale, and point GO as an important candidate material for the fabrication of ultra-small (<500 nm^2) electronic synapses fulfilling the integration density requirements of neuromorphic systems.

Keywords: electronic synapse, resistive switching, synaptic plasticity, graphene oxide, spray coating, conductive atomic force microscopy

Main text

Resistive switching (RS) is a phenomenon occurring in different metal/insulator/metal (MIM) devices that consists on the adjustment of their electrical resistance depending on the history of electrical stresses applied.[1] Depending on the materials employed, MIM devices can exhibit: i) two stable resistive states (often called non-volatile RS), which has been used to fabricate binary electronic memories;[2] and ii) one stable and one unstable resistive state (often called threshold RS), which is being explored for the fabrication of electronic neurons, i.e. devices for signal integration and electrical spike generation in ANNs; [3] and iii) multiple

stable resistive states (often called analogue RS), which is being explored for the fabrication of electronic synapses, i.e. devices that define the strength of the connection between electronic neurons in artificial neural networks (ANNs).[3] The fabrication of state-of-the-art electronic memories and ANNs using MIM-like RS devices requires high integration density (>10^{10} devices/mm^2),[4] meaning that the RS must be demonstrated in ultra-small devices (<100 nm^2).[5-7] The smallest memristors fabricated have sizes of 2 nm × 2 nm and had a Pt/TiO_2/HfO_2/Pt structure[6], but just few RS cycles were demonstrated and the switching voltages presented a high variability (>2V). Ref.[7] presented a complete statistical analysis demonstrating RS in 10 nm × 10 nm memristors in with TiN/Hf/HfO_2/TiN structure. However, observing RS in small areas <100nm^2 is extremely challenging, and the number of studies in this direction is very scarce.

One simple and powerful strategy to explore the presence of RS in a materials system is the use of scanning probe microscopy (SPM) techniques, as they allow to characterize multiple nano-sized MIM cells (with sizes ranging from 1 nm^2 [8] to 50 nm^2 [9]). SPM techniques like scanning tunnelling microscopy (STM) and conductive atomic force microscopy (CAFM) have been often employed to study binary RS in different materials;[10-11] however, the use of SPM techniques to explore other types of RS (i.e. analogue, threshold) for the fabrication of electronic synapses and neurons is still incipient. Refs.[10-11] used the tip of a STM as a top electrode to analyse nanogap-based Ag_2S and Cu_2S atomic switches, and observed short term plasticity (STP, i.e. volatile changes in resistance that recover after few milliseconds or seconds)[12] and long term plasticity (LTP, i.e. non-volatile changes in resistance that remain stable for minutes or days)[13]. However, in Refs.[10-11] the STM probe did not physically contact the device surface, therefore the electrical characteristics were affected by the nanogap between tip and sample, which can be very unstable and produce high point-to-point variability. On the contrary, CAFM provides physical and stable contact

between the tip and the sample, as well as accurate control of the contact force (F_C) between them,[14] and it is overall more suitable than STM to form nano-sized MIM contacts.

Here we use and advanced CAFM-based setup to study of nano-synaptic response in graphene oxide (GO) films prepared by liquid phase exfoliation (LPE)[15] and deposited by spray coating on metal-varnished Si wafers. The CAFM Pt tip is connected to a Keysight B1500A semiconductor parameter analyser (SPA), so that ramped voltage stresses (RVS) and sequences of pulsed voltage stresses (PVS) can be applied locally, and the current signal can be simultaneously measured in situ within a wide range (from ±1 pA to ±1 mA).[16-17] Our experiments indicate that nanosized (~50 nm^2) metal/GO/metal cells exhibit the coexistence of different synaptic responses enabled by the presence of volatile RS, such as potentiation and paired pulse facilitation (PPF) at low current levels <1 μA, controllable excitatory post-synaptic current (EPSC), smooth potentiation and depression, and non-volatile bipolar RS necessary to achieve reproducible LTP.

We use GO for multiple reasons. First, the traditional materials employed in RS devices are mainly transition metal oxides (TMO), but they are having difficulties to exhibit analogue and threshold RS; therefore, new materials need to be explored,[18-20] and GO has already shown non-binary RS[21-23] in large devices (areas >7000 μm^2). Second, GO can be prepared inexpensively via LPE method, plus the spray coating technique developed in our laboratory allows conformal coating of surfaces with complex shapes;[24] this approach is very attractive from an industrial point of view. And third, GO is a two-dimensional (2D) layered material (LM) that holds multiple properties that make it very attractive for the fabrication of solid-state electronic devices and integrated circuits, such as high flexibility and transparency.[25-26] Previous studies have reported that GO-based materials exhibit multiple RS-related phenomena, including STP, LTP, STDP in modified GO based transistor,[21] STP and PPF in Ag/N-GOQD/Pt (where N-GOQD stands for N-doped GO quantum dots)[22] and EPSC, PPF

in crossbar arrays made of yarn coated with GO;[23] however, the sizes of all GO-based memristive devices reported to date were very large (>7000 μm^2),[21-23] and demonstrations of electro-synaptic behaviours at the nanoscale are required for GO to be used in high-density ANNs (>10^{10} devices/mm^2). In this context, our study demonstrates that GO can exhibit multiple nano-synaptic electronic phenomena at the nanoscale, and therefore it could be attractive for the fabrication of ultra-scaled electronic synapses and neurons.

We prepare GO flakes by a wet chemical method as detailed in Methods. Transmission electron microscopy (TEM) image (**Figure 1**a) show that they are continuous over areas >20 μm^2. The GO flakes are then deposited on Au-varnished SiO_2 wafers using a spray-coater (see Methods), which is a cheap technique that allows scalable fabrication of devices.[27] The GO thickness on the metal can be controlled by adjusting the pressure of the spray-coater and the spraying time. Figure 1b shows a topographic AFM map of the surface of a GO/Au/SiO_2 wafer. The root mean square (RMS) roughness of the flat regions (i.e. without wrinkles) is ~2.75 nm; this value, which is extracted by processing the topographic AFM images offline, using the NanoScope Analysis AFM software, is similar to that of GO films prepared by spin coating.[26] The ability of spray-coating technique to coat any complex surface is demonstrated using bulk Pt tips as substrate for GO deposition. We use Raman spectra and wettability measurements to confirm the existence of oxygen-containing functional groups and hydrophilic nature (respectively, see Supplementary Figure S1a-c). Figs. 1c-d are scanning electron microscopy (SEM) images of an as-received bulk Pt tip (without GO) and a GO-coated bulk Pt tip, respectively. These images show that conformal GO coating is achieved (recognized by the formation of wrinkles). Similar results are readily achieved in other CAFM tips with different geometries (see Supplementary Figure S1d).

To construct nanosized GO-based memristive electronic synapses, we use two different configurations. *1)* A bulk Pt tip placed at a single location on the surface of a GO/Au/SiO_2

wafer, which leads to Pt/GO/Au nano-synapses with an effective area (between tip and sample) <50 nm^2,[9] given that the typical radius of the Pt tips is ~8 nm (see Supplementary Figure S2). *2)* GO-coated bulk Pt tip placed on the surface of a Cu film, which leads to Pt/GO/Cu nano-synapses with slightly larger effective areas <500 nm^2, as the radius of the GO-coated tip is larger than that of the uncoated tip, due to the additional thickness of the GO film to the Pt tip (~65 nm, as demonstrated by close inspection of SEM images, see Supplementary Figure S2). Both types of structures are shown schematically in **Figure 2**. More details about the estimation of the effective size of the nano-synapses is provided in Supplementary Note 1.

Figure 2b plots the current vs. voltage (*I-V*) curves collected on a single location of the Pt/GO/Cu nano-synapse in Figure 2a when exposed to a sequence of 20 RVS from 0 V to 5 V across the Pt and Cu electrodes (V_{TIP}), using a standard CAFM (see Figure 2d). During the forward *I-V* curves (blue) only electrical noise is initially detected (at V_{TIP} <1 V). At V_{TIP} ~1 V the currents start to increase progressively. At V_{TIP} ~3 V the currents increase abruptly until reaching the saturation level of the CAFM (±5 nA). The backward *I-V* curves (dark yellow) show a current shift towards lower potentials, indicating that the resistivity of the Pt/GO/Cu nano-synapse has decreased. The fact that the currents during the backward *I-V* curve vanish at low voltages (V_{TIP} <0.5 V), and that the next forward *I-V* curve exhibits similar currents to the previous forward one, indicate that the RS phenomenon is volatile. The variability from one cycle to another, evaluated through the mean value (μ) and standard deviation (σ) of the switching voltages,[28] is relatively low (2.99 ± 0.32 V for V_{SET} and 0.69 ± 0.28 V for V_{RESET}), as shown in Figure 2c, and comparable to that of TMO based memristors,[29] indicating the good reproducibility and reliability of the threshold RS behaviour. We observed similar threshold RS characteristics for Pt/GO/Au synapses (see Supplementary Figure S3).

To have dynamic information about the switching processes (i.e. set and reset) we apply PVS to the metal/GO/metal nano-synapses by connecting a SPA to the tip of the CAFM (see schematic in Figure 2e). When applying fast (<500 ns) PVS, we present the data for the Pt/GO/Au nano-synapses (Figure 2f) because the dynamic current signals are more stable and reproducible than for the Pt/GO/Cu ones. We apply PVS with a pulse width (W) ~500 ns, V_{TIP} ranging from ~2.5 V (V_{PULSE}) and 0 V (V_{READ}), and different interval times (T) ~19.3, 9.3 and 4.3 μs (Figure 2g-i). Our experiments indicate that when longer T ~19.3 μs is used (Figure 2g), the currents flowing across the Pt/GO/Au nano-synapses can complete its relaxation (back to initial current level) after each pulse. On the contrary, when applying shorter T ~4.3 μs (Figure 2i), the currents relaxation is incomplete and the Pt/GO/Au nano-synapses are erratically potentiated.

By adjusting the width and interval of the PVS (W ~100 μs and T ~100 μs), analogue potentiation and PPF at wide current ranges from ~40 nA to ~100 μA is achieved when applying different pulse amplitudes (V_{PULSE} = 3, 5 V and V_{READ} = 0 V), as shown in **Figure 3**a and 3d. The speed of the potentiation can be adjusted by tuning the pulse amplitude, and the current across different Pt/GO/Au nano-synapses is similar, indicating that the device-to-device variability is low. The observation of reproducible analogical potentiation at low current levels (<1 μA) across ultra-small areas <50 nm^2 represent a significant advancement in terms of write current and integration density compared to the previous literature in this field (see Figure 3e). We would like to clarify that in this study we demonstrate the lowest current during the write pulse (not read pulse) because the read currents are below the intrinsic noise of the SPA operated in pulse mode (i.e. ~1 μA), and therefore they cannot be measured with this setup. The median power consumption in a potentiation cycle (P_{MEDIAN}), defined as the amplitude of the pulse (V_{PULSE}) multiplied by the median current during the potentiation cycle (I_{MEDIAN}), is 3 μW, one of the lowest values reported in the literature (see

Supplementary Table S3). At such current levels the potentiation happens in a linear manner (see Figure 3f), which is also a desired feature in electronic synapses for ANNs.[30] The factor ~2 variability of the currents that we observed between different metal/GO/metal synapses is small compared to state-of-the-art memristors, in which currents fluctuations ranging from 5[31] to 1000[29] from one device to another have been reported. Pt/GO/Au nano-synapses also exhibit EPSC response, i.e. transmission of spikes or action potentials from the pre-synaptic neuron (Pt) to the post-synaptic neuron (Au) across the GO synapse. Figure 3g shows four groups of presynaptic pulses with amplitudes of 3, 3.5, 4, 4.5, 5 V and T = 100 μs applied to the bulk Pt tip. The EPSC increases with both amplitude and number of presynaptic pulses, Figure 3g. This type of EPSC response is similar to that observed in biological excitatory synapses.[32] Corresponding excitatory responses (peak values) in each pulse (Figure 3h) indicate that the conductance of the Pt/GO/Au nano-synapses starts to increase from the second group, and exhibits an overall increasing trend with the number of groups (upward/downward instabilities from one pulse to another have been observed, which are normal and similar to those in multiple other studies,[33-36] although the overall trend is increasing with the number of groups). There is a conductance decrease after one group with a stop time of 4 ms, indicating a relaxation process of the nano-synapses.

When the polarity of the PVS is inverted (i.e. V_{PULSE} = -4 V, with T = 100 μs and W = 100 μs), the Pt/GO/Au nano-synapses exhibit non-volatile conductance increase under long (2000) sequences of PVS up, **Figure 4**a. When the bias is switched-off the conductance does not recover its initial value. The conductance of the Pt/GO/Au nano-synapses can then be decreased by applying PVS with opposed polarity (i.e. V_{PULSE} = 4 V). This is seen in Figure 4a, which shows the variability of the currents registered in each conductance state (each box includes 200 data points). These electrical measurements reveal that the Pt/GO/Au nano-

synapses exhibit stable long-term potentiation and depression, necessary to implement LTP[13,37].

Investigating the RS mechanism in these ultra-scaled (<50 nm^2) nano-synapses, which requires the use of chemical tools with nanoscale lateral resolution [38] or first principles calculations [39], is out of the scope of this investigation due to their extreme complexity. The goal of SPM-based investigations in the field of RS (like this one) is to demonstrate that the nano-synaptic response can be observed in small areas <50 nm^2, and to describe the quality of the RS phenomenon (i.e. shape of the electrical plots). Multiple studies have claimed the switching mechanism in metal/GO/metal memristors by interpreting electrical signals [21-23] and chemical techniques with low (>5 μm) lateral resolution.[22, 40] While these are not the recommended methods to study the RS mechanism (only chemical tools with nanoscale lateral resolution or first principles calculations are),[41] this approach can provide some preliminary insights. Using a similar approach, our electrical measurements presented in Figures 2-4 allow us to make reasonable suggestions. First, the fact that the threshold (i.e. volatile) resistive switching (Figures 2-3) is only observed when the potentiation is realized by applying positive voltage to the Pt electrode (see Supplementary Figure S4a) makes us believe that this behaviour is related to the formation of oxygen vacancies in the GO film. Under these biasing conditions: i) the O^{2-} ions, which have a low (<0.7 eV) activation energy,[42] try to move towards the Pt electrode; ii) the Pt^{+} ions, which have a high (>0.7 eV) activation energy,[43] are not be able to move; and iii) the Cu^{+} ions (in Pt/GO/Cu devices) and Au^{+} ions (in Pt/GO/Au devices) are pushed away from the GO film. Therefore, the most probably atomic rearrangement is the movement of O^{2-} ions (including the transformation between insulating sp^3 and conducting sp^2), which should result in a local increase of the conductance.[26,44] And second, the fact that the non-volatile RS is only observed when the potentiation is realized by applying negative voltage to the Pt electrode (see Supplementary

Figure S4b) makes us believe that is generated by the penetration of metal in to the GO film, i.e. Cu^+ ions in Pt/GO/Cu devices and Au^+ ions in Pt/GO/Au devices. Under these biasing conditions: i) the O^{2-} ions, which have a low activation energy,[42] try to move towards the Cu or Au electrode; ii) the Pt^+ ions, which have a high activation energy,[43] are not be able to move; and iii) the Cu^+ ions (in Pt/GO/Cu devices) and Au^+ ions (in Pt/GO/Au devices), which diffusivity is much (3~4 times) higher than that of Pt,[45] can penetrate in the GO film. Therefore, the switching is enabled by a combination of movement of O^{2-} ions towards the Cu or Au electrode, plus penetration of Cu^+ or Au^+ ions in the GO film, as observed in many other devices with similar structure and electrodes.[45] It is also important to consider that the GO film has been synthesized via LPE, which results on the formation of many defects at the junctions between the 2D flakes,[46] favouring reversible ion migration at those sites at lower electrical fields. In any case, readers must keep in mind that only the use of chemical tools with nanoscale lateral resolution [38] or first principles calculations[39] can truly demonstrate the RS mechanism (and for this reason we do we prefer not to make strong claims about a specific resistive switching mechanism based on speculative schematics and intuition, as many authors often do).

In order to further understand the conduction across the metal/GO/metal nano-synapses, we carry out additional experiments and calculations. The maximum conductance of the Pt/GO/Au nano-synapses during the potentiation and depression cycles is ~1.5 μS, Figure 4a, well below the quantum conductance G_0 = 77.5 μS [47]. This indicates that RS is driven by the accumulation of defects inside the dielectric, without forming a conductive nanofilament (CNF) across the GO film. In order to validate this, the width of the pulses is increased (i.e. T = 20 ms and W = 10 ms). When the conductance of the Pt/GO/Au nano-synapse surpasses G_0 the depression becomes sharper (see Figure 4b). This is related to the rupture of a CNF at the transition to sub-G_0 conductance. The non-volatility of the RS when potentiating the

Pt/GO/Au nano-synapses by applying a negative voltage to the Pt electrode is confirmed via RVS, which exhibit V_{SET} ~ -4 V and V_{RESET} ~5.5 V (see Figure 4c,d). The switching voltages can be further decreased when using Cu as electrode (instead Au), as it has a higher diffusivity.[48] Figure 4e shows that Pt/GO/Cu nano-synapses exhibit non-volatile bipolar RS with V_{SET} ~0.99 V and V_{RESET} ~0.78 V. The variability of the V_{SET} and V_{RESET} from one cycle to the other is consistent with that observed in other RS devices,[37] and does not represent a problem for their use as electronic synapse in ANNs.[41] The fact that the bipolar RS is observed at conductance < G_0 (Figure 4c,d) also indicates that no CNF is completely formed across the GO film. We calculate the relative temperature increase in the metal/GO/metal nano-synapses during the *I-V* curves in Figure 4c, using the model in Ref.[49], as follows the 3D heat equation presented in Supplementary Note 2. Our calculations (see Supplementary Note 2) indicate that at those current regimes, thermal effects are negligible. The temperature increases for the maximum current ~30 μA (at ~6 V) is <320 K. This observation further points to ionic migration being responsible for RS, and that no CNF is formed in either volatile (Figures 2 and 3) and non-volatile (Figure 4a) regimes.

In conclusion, we have probed the presence of nano-synaptic response in GO films at ultra-small areas (<500 nm^2) by using a CAFM connected to a semiconductor parameter analyser. The GO films were deposited on metal-coated wafers and bulk Pt tips using an industry-compatible spray-coating methodology, achieving excellent conformal coating. The metal/GO/metal nano-synapses emulate potentiation and PPF at low current levels <1 μA, controllable EPSC and controllable long-term potentiation and depression, and non-volatile bipolar RS (necessary to emulate LTP) at higher current ranges. Both RS mechanisms take place at very low operating currents (i.e. conductance below G_0, i.e. non-filamentary mechanism), resulting in a very low power consumption (~3 μW). Our work provides a facile method to detect nano-synaptic response in different types of materials and indicates that GO

may be an excellent RS medium to fabricate small area (<50 nm^2) memristive electronic synapses (operating at low current ranges) for high-density ANNs.

Experimental Section

GO Preparation: GO is prepared as follows. **Step1: Pre-treatment.** Graphite Flakes (3g, Sigma-Aldrich) are mixed with 98% sulfuric acid (H_2SO_4, 12 mL), potassium persulfate ($K_2S_2O_8$, 2.5 g), and phosphorus pentoxide (P_2O_5, 2.5 g) and the mixture is heated to 80 °C for 5 hours. Afterwards, the mixture is diluted with de-ionized water (H_2O, 0.5 L), filtered and washed with de-ionized H_2O (three times) to remove the residual acid. The resultant is dried at 80 °C overnight. **Step2**: **Oxidation** by Hummers' method.[50] The pre-treated graphite flakes are transferred into 98% H_2SO_4 (120 mL) cooled in an ice bath. Then, potassium permanganate ($KMnO_4$, 15 g) is added gradually under stirring to keep the temperature < 20 °C. The mixture is stirred at 35°C for 4 h, and diluted with de-ionized (DI) H_2O (250 mL). Afterwards the mixture is stirred for 2 h at 90 °C, followed by the addition of DI H_2O (0.7 L). Hydrogen peroxide (H_2O_2, 30%, 20 mL) is then added, and the resulting brilliant-yellow mixture is filtered and washed with hydrochloric acid aqueous solution (HCl, 10 wt%) to remove metal ions. GO is then washed repeatedly in order to remove residual acid with H_2O until neutral pH., then diluted to yield a GO dispersion with concentration ~5 g/L. Immediately before spray coating, the GO is diluted with ethanol to a give a final concentration~0.5 g/L. After the synthesis of the GO the flakes are dispersed in ethanol at a concentration ~0.5 mg/ml to make the GO ink.

Spray coating: We used an air-assist atomiser (Specialty Coating Systems Precisioncoat V) to deposit the GO ink. We position an array of ten nanoprobes at a distance ~8 cm under the

spray nozzle. The flow rate is set to 13.5 ml/min to control the speed of liquid ejection from the spray nozzle. An atomisation pressure (i.e. the gas pressure applied across the liquid ejected from the spray nozzle) ~9 psi is used. We move the nozzle at a speed ~12.7 cm/s across the array of nanoprobes to cover the probes in a coating of GO ink. The coating process is undertaken at room temperature (20°C) to minimize the surface roughness. We pass the spray nozzle over the array of nanoprobes five times (i.e. five coating layers) to create the GO film. The same conditions are used to coat the SiO_2 wafers.

Electrical measurements: As our nanoelectronic measurements are not standard, additional hardware is needed to apply PVS and measure *I-V* curves with wide current range (±1 pA to ±1 mA). We thus utilize three CAFM systems: 1) NX-HighVac from Park Systems, 2) Bruker Dimension Icon from Bruker, 3) Multimode V from Veeco. All are equipped with Pt tips from Rocky Mountain (model RMN-25PT300B), with a tip radius <8 nm and a nominal spring constant~18 N/m. For all CAFM tests, the voltages are applied to the CAFM tip, while keeping the sample substrate grounded. The use of solid bulk Pt tips is extremely important to ensure high stability of the tips (i.e. metal-varnished Si tips degrade easily after some measurements) and makes the data measured here highly reliable. When measuring PVS or *I-V* curves with enhanced voltage and current ranges, electrical stresses are applied to the CAFM tip using the SMU1 of a B1500A SPA, and the post-synaptic currents are collected with the SPA SMU2, Figure 2e. The nominal contact force between tip and sample during RVS and PVS is ~2 nN, in order to avoid GO film deformation. The contact resistance between tip and a metallic sample is ~ 10 Ω, which is negligible compared to the high resistance detected in the metal/GO/metal device due to the insulating nature of the GO film.

Supporting Information

Supporting Information is available from the Wiley Online Library or from the author

Acknowledgements

We acknowledge funding by the Ministry of Science and Technology of China (grant no. BRICS2018-211-2DNEURO), the National Natural Science Foundation of China (grants no. 11661131002, 61874075), the Ministry of Finance of China (grant no. SX21400213), the Jiangsu Planned Projects for Postdoctoral Research Funds of China (Grant No. 7131712019), the 111 Project from the State Administration of Foreign Experts Affairs of China, the Collaborative Innovation Centre of Suzhou Nano Science & Technology, the Jiangsu Key Laboratory for Carbon-Based Functional Materials & Devices, the Priority Academic Program Development of Jiangsu Higher Education Institutions, the Isaac Newton Trust, the EU project CareRAMM, EU Graphene Flagship, ERC Grants Hetero2D and MINERGRACE, EPSRC Grants EP/K01711X/1, EP/K017144/1, EP/N010345/1, EP/M507799/1, EP/L016087/1, EP/R511547/1, EP/P02534X/2, EP/T005106/1 and a Technion-Guangdong Fellowship.

Received: ((will be filled in by the editorial staff))
Revised: ((will be filled in by the editorial staff))
Published online: ((will be filled in by the editorial staff))

References

[1] Ielmini, D.; Waser, R. Resistive switching: from fundamentals of nanoionic redox processes to memristive device applications. *Wiley-VCH* Germany (2016).

[2] Chen, A. *et al.* Non-volatile resistive switching for advanced memory applications. *IEEE International Electron Devices Meeting* DOI: 10.1109/IEDM.2005.1609461 (2005).

[3] Rao, K. D. M.; Sagade, A. A.; John, R.; Pradeep, T.; Kulkarni, G. U. Defining switching efficiency of multilevel resistive memory with PdO as an example. *Adv. Electron. Mater.* **2**, 1500286 (2016).

[4] Xia, Q.; Yang, J. J. Memristive crossbar arrays for brain-inspired computing. Nat. Mater. 18, 309-323 (2019).

[5] Yang, J. J. *et al.* Memristive switching mechanism for metal/oxide/metal nanodevices. *Nat. Nanotechnol.* **3**, 429 (2008).

[6] Pi, S. *et al.* Memristor crossbar arrays with 6-nm half-pitch and 2-nm critical dimension. *Nat. Nanotechnol.* **14**, 35-39 (2019).

[7] B. Govoreanu et al. 10x10 nm^2 Hf/HfO_x crossbar resistive RAM with excellent performance, reliability and low-energy operation. *IEEE IEDM* DOI: 10.1109/IEDM.2011.6131652 (2011).

[8] Lanza, M. *et al.* Crystallization and silicon diffusion nanoscale effects on the electrical properties of Al2O3 based devices. *Microelectron. Eng.* **86**, 1921-1924 (2009).

[9] Frammeblsberger, W., Benstetter, G., Kiely, J., Stamp, R. C-AFM-based thickness determination of thin and ultra-thin SiO2 films by use of different conductive-coated probe tips. *Appl. Surf. Sci.* **253**, 3615-3626 (2007).

[10] Nayak, A. *et al.* Controlling the synaptic plasticity of a Cu_2S gap-type atomic switch. *Adv. Funct. Mater.* **22**, 3606-3613 (2012).

[11] Ohno, T. *et al.* Short-term plasticity and long-term potentiation mimicked in single inorganic synapses. *Nat. Mater.* **10**, 591-595 (2011).

[12] Zucker, R. S. Short-term synaptic plasticity. *Annu. Rev. Neurosci.* **12**, 13–31 (1989).

[13] Hyvarinen, A. New approximations of differential entropy for independent component analysis and projection pursuit. *In Advances in Neural Information Processing Systems 10, NIPS Proceedings* 273–279 (1997).

[14] Lanza, M. in Conductive Atomic Force Microscopy: Application in Nanomaterials. Wiley-VCH, 2017.

[15] Hernandez, Y. *et al.* High-yield production of graphene by liquid-phase exfoliation of graphite. *Nat. Nanotechnol.* **3**, 563-568 (2008).

[16] Hui, F., Lanza, M. Scanning probe microscopy for advanced nanoelectronics. *Nat. Electron.* **2**, 221-229 (2019).

[17] Iglesias, V., Jing, X., Lanza, M. in Conductive Atomic Force Microscopy: Application in Nanomaterials (ed. Lanza, M.) Ch. 10 (Wiley-VCH, 2017).

[18] Hui, F. *et al.* Graphene and related materials for resistive random access memories. *Adv. Electron. Mater.* **3**, 1600195 (2017).

[19] Ott, A. K. *et al.* Tetrahedral amorphous carbon resistive memories with graphene-based electrodes. *2D Mater.* **5**, 045028 (2018).

[20] Ahmed, T. *et al*. Optically stimulated artificial synapse based on layered black phosphorus. *Small* **15**, 1900966 (2019).

[21] Yang, Y. *et al.* Long-term synaptic plasticity emulated in modified graphene oxide electrolyte gated IZO-based thin-film transistors. *ACS Appl. Mater. Interfaces* **8**, 30281-30286 (2016).

[22] Sokolov, A. S. *et al.* Silver-adapted diffusive memristor based on organic nitrogen-doped graphene oxide quantum dots (N-GOQDs) for artificial biosynapse applications. *Adv. Funct. Mater.* **29**, 1807504 (2019).

[23] Park, Y. et al. Reduced graphene oxide-based artificial synapse yarns for wearable textile device applications. *Adv. Funct. Mater.* **28**, 1804123 (2018).

[24] Ibrahim, A. F. M., Lin, Y.S. Synthesis of graphene oxide membranes on polyester substrate by spray coating for gas separation. *Chem. Eng. Sci.* **190**, 312-319 (2018).

[25] Backers, C. *et al.* Production and processing of graphene and related materials. *2D Mater.* **7**, 022001 (2020).

[26] Romero, F. J. *et al.* Laser-fabricated reduced graphene oxide memristors. *Nanomaterials* **9**, 897 (2019).

[27] Torrisi, F., Carey, T. Graphene, related two-dimensional crystals and hybrid systems for printed and wearable electronics. *Nano Today* **23**, 73-96 (2018).

[28] Adam, G. C. *et al.* 3-D Memristor Crossbars for Analog and Neuromorphic Computing Applications. *IEEE Trans. Electron Devices* **64**, 312–318 (2017).

[29] Fantini, A. *et al.* Lateral and vertical scaling impact on statistical performances and reliability of 10nm TiN/Hf(Al)O/Hf/TiN RRAM devices. *VLSI Technol.* doi: 10.1109/VLSIT.2014.6984433 (2014).

[30] Zhang, W. *et al*. Analog-type resistive switching devices for neuromorphic computing. *Phys. Status Solidi RRL* 1900204 (2019).

[31] Chen, S. C. *et al.* Wafer-scale integration of 2D materials in high-density memristive crossbar arrays for artificial neural networks. *Nat. Electron.* **3**, 638-645 (2020).

[32] Xu, W. *et al.* Organic core-sheath nanowire artificial synapses with femtojoule energy consumption. *Sci. Adv.* **2**, e1501326 (2016).

[33] Wang, Z. *et al.* Memristors with diffusive dynamics as synaptic emulators for neuromorphic computing. *Nat. Mater.* **16**, 101-108 (2017).

[34] S. H. Jo, et al. Nanoscale memristor device as synapse in neuromorphic systems. *Nano Lett.* **10**, 1297-1301 (2010).

[35] Kim, S. *et al.* Analog synaptic behavior of a silicon nitride memristor. *ACS Appl. Mater. Interfaces* **9** 40420-40427 (2017).

[36] Yan, X. *et al.* Memristor with Ag-cluster-doped TiO_2 films as artificial synapse for neuroinspired computing. *Adv. Funct. Mater.* **28**, 1705320 (2018).

[37] Shi, Y. *et al.* Electronic synapses made of layered two-dimensional materials. *Nat. Electron.* **1**, 458-465 (2018).

[38] C. Yoshida, K. Kentaro, Y. Takahiro, S. Yoshihiro, *Appl. Phys. Lett.* **2008**, *93*, 042106.

[39] Szot, K., Speier, W., Bihlmayer, G. & Waser, R. Switching the electrical resistance of individual dislocations in single-crystalline SrTiO3. Nature Mater. 5, 312–320 (2006).

[40] Website of Thermo Fisher Scientific, www.thermofisher.com/ (accessed: March 2021).

[41] Lanza, M. *et al.* Recommended methods to study resistive switching devices. *Adv. Electron. Mater.* **5**, 1800143 (2018).

[42] Pirrotta, O. et al. Multi-scale modelling of oxygen vacancies assisted charge transport in sub-stoichiometric TiO_x for RRAM application. *IEEE Proc. Int. Conf. Simul. Semicond. Processes Devices* DOI: 978-1-4799-5288-5/14/. (2014).

[43] Yang, Y. et al. Observation of conducting filament growth in nanoscale resistive memories. Nat. Commun. 3, 732 (2012).

[44] Porro, S., Accornero, E., Pirri, C.F., Ricciardi, C. Memristive devices based on graphene oxide. *Carbon* **85**, 383-396 (2015).

[45] Zhuge, F. *et al.* Mechanism of nonvolatile resistive switching in graphene oxide thin film. *Carbon* **49**, 3796-3802 (2011).

[46] Jing, X. et al. Engineering field effect transistors with 2D semiconducting channels: Status and prospects. *Adv. Funct. Mater.* **30**, 1901971 (2020).

[47] Pan, C. *et al.* Model for multi-filamentary conduction in graphene/hexagonal-boron-nitride/graphene based resistive switching devices. *2D Mater.* **4**, 025099 (2017).

[48] Yang, Y., *et al.* Electrochemical dynamics of nanoscale metallic inclusions in dielectrics. *Nat. Commun.* **5**, 4232 (2014).

[49] Maestro, M. *et al.* Unipolar resistive switching behavior in Al_2O_3/HfO_2 multilayer dielectric stacks: fabrication, characterization and simulation. *Nanotechnology* **31**, 135202 (2020).

[50] Hummers, W. S., Offeman, R. E. Preparation of graphitic oxide. *J. Am. Chem. Soc.* **80**,

1339 (1958).

[51] International Technology Roadmap for Semiconductors, 2013 Edition, Process Integration, Devices, and Structures section, http://www.itrs.net (accessed February 11th 2015).

List of Figures

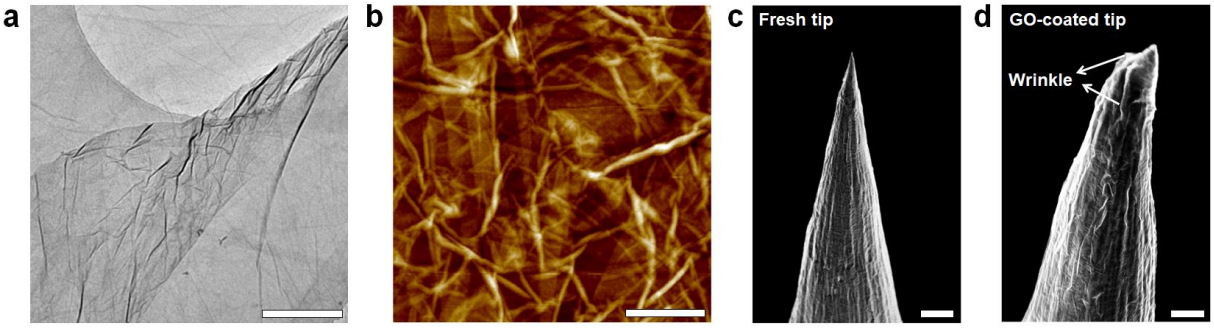

Figure 1. Morphological characterization of spray-coated GO. **a**, TEM image of GO flake. Scale bar 500 nm. **b**, Topographic AFM map of a GO/Au/SiO_2 wafer. Scale bar 500 nm. The color scale (Z-axis) is: black 0 nm, white 20 nm. **c, d,** SEM images of as-received Pt tip (without GO coating) and GO-coated Pt tip (after coating). Scale bars are 2.5 µm in **c** and 1 µm in **d**.

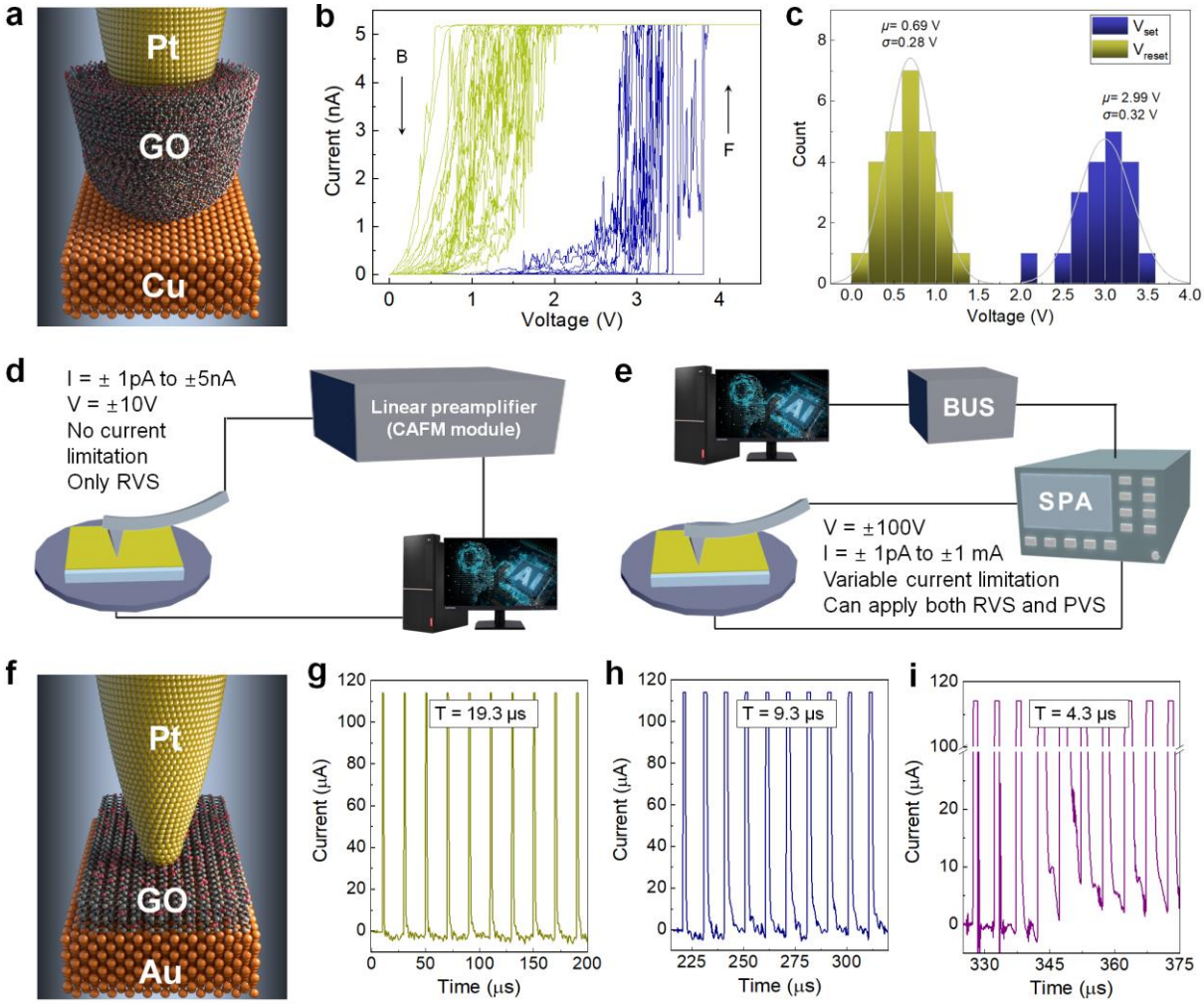

Figure 2. Electrical measurement of metal/GO/metal. **a,** Schematic GO-coated Pt tip on Cu, forming a Pt/GO/Cu nano-synapse with area <50 nm^2. **b,** *I-V* sweeps in a Pt/GO/Cu nano-synapse showing volatile RS. **c,** Statistical analysis of the switching voltages of Pt/GO/Cu nano-synapse. **d, e,** Schematic diagrams of standard CAFM and a CAFM connected to a SPA, respectively. **f,** Schematic of a Pt tip on GO/Au/SiO_2, forming a Pt/GO/Au nano-synapse with area <50 nm^2. **g, h, i,** Current signal driven by a Pt/GO/Au nano-synapse when applying PVS with common width (W = 500 ns) and amplitude (V_{PULSE} = 2.5 V), and T = 19.3, 9.3, 4.3 μs, respectively.

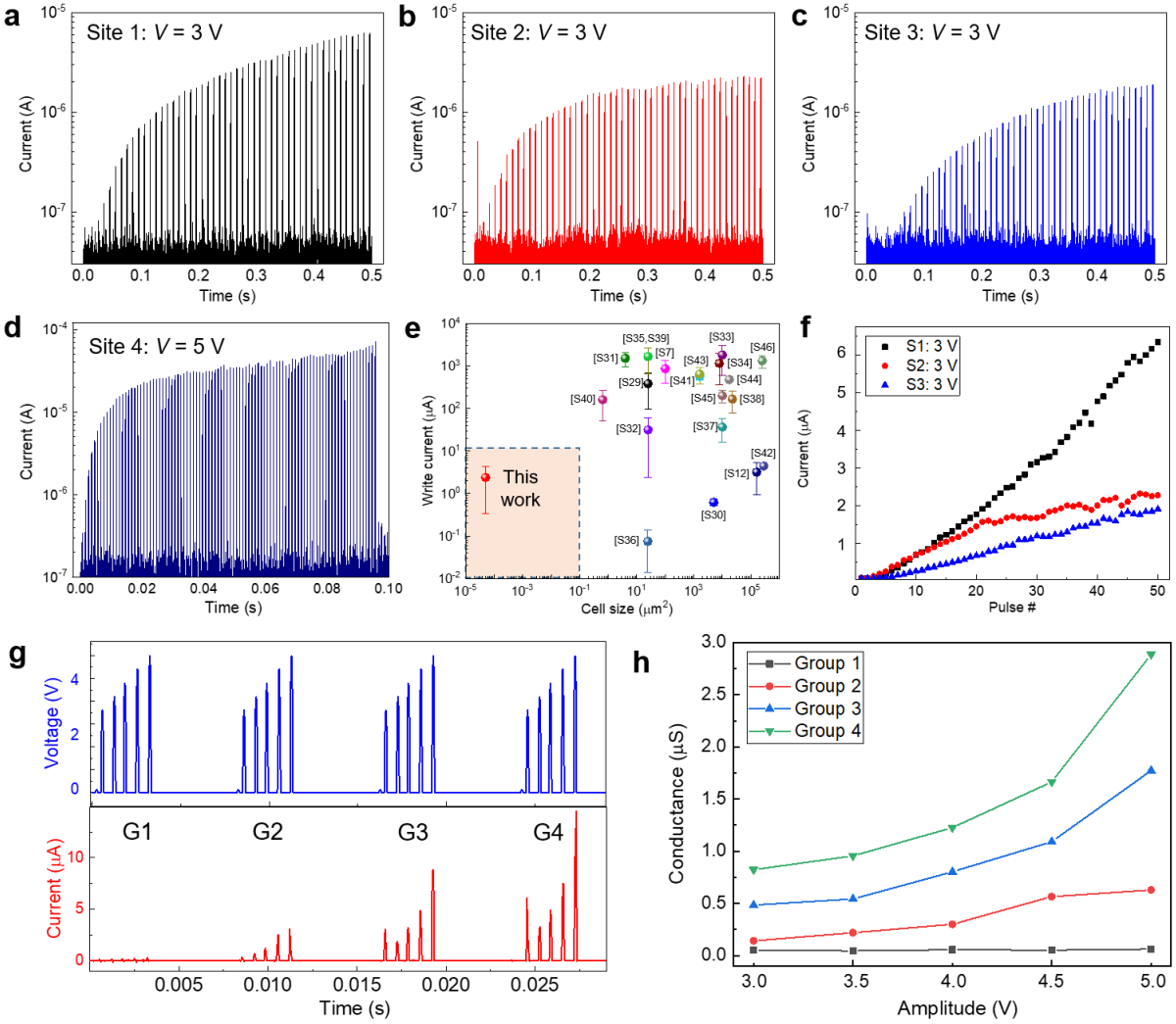

Figure 3. Writing current and EPSC in Pt/GO/Au nano-synapses. **a, b, c,** Current signals driven by 3 Pt/GO/Au nano-synapses when applying PVS with common W = 1 ms, T = 2 ms, V_{PULSE} = 3 V. **d,** Current signals driven by Pt/GO/Au nano-synapses when applying PVS with common W = 100 μs, T = 1 ms, and V_{PULSE} = 5 V. **e**, Writing current vs. cell size for 20 memristive synapses reported in literature and this work. The Refs.[S7,S12,S29-S46] are indicated in the Supplementary Information (see also Table S3). The orange region outlines the values closer to the technological requirements, as defined in Ref.[51]. **f,** Writing current vs. pulse number for the plots in **a-c** showing that potentiation takes place in a linear manner at low currents <1 μA. **g,** EPSC response (bottom) measured in one Pt/GO/Au nano-synapse when applying four groups of PVS (G1-G4), each with amplitudes of 3, 3.5, 4, 4.5, 5V (top). **h,** Average conductance change in the Pt/GO/Au nano-synapse for PVS of different amplitude when repeating the experiment in **g** for 4 times in the same synapse.

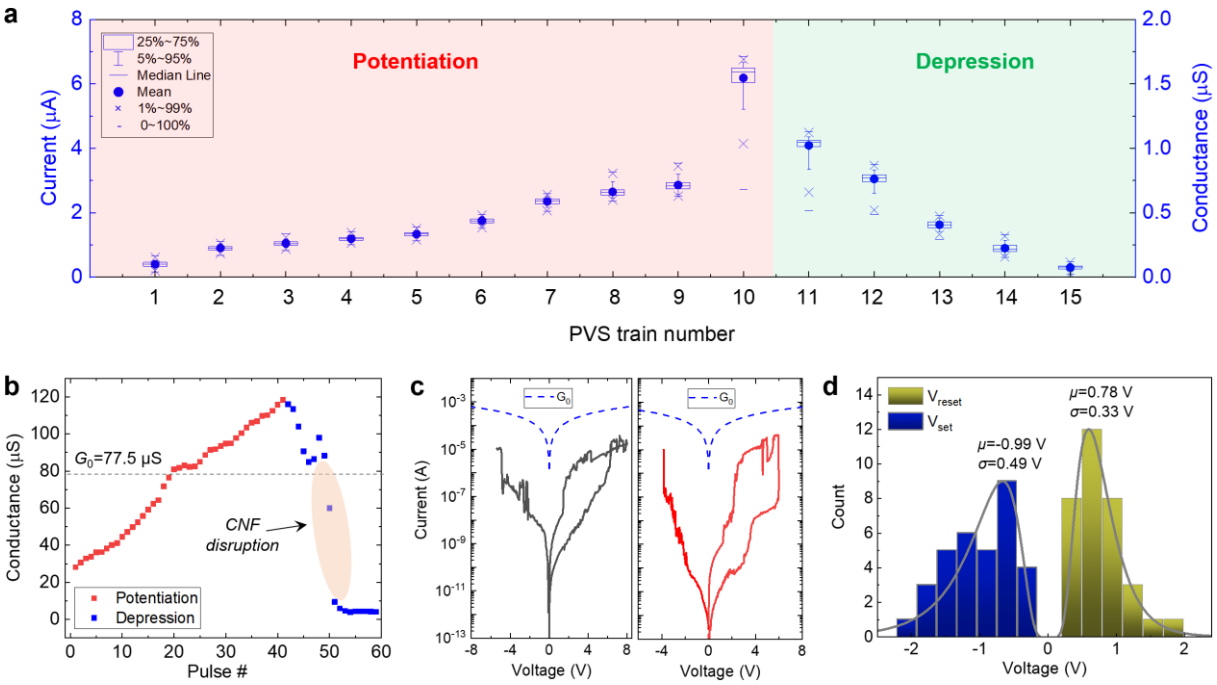

Figure 4. Non-volatile RS in Pt/GO/Au nano-synapses. **a,** Current driven by a Pt/GO/Au nano-synapse when applying PVS trains with V_{PULSE} = -4 V (potentiation, trains 1-10) and V_{PULSE} = 4 V (depression, trains 11-15) to the Pt electrode (W = 100 μs, T = 100 μs). The value of the conductance is also indicated. **b**, Conductance of a Pt/GO/Au nano-synapse when applying PVS, showing that above G_0 the disruption is sharp, indicating that a filament was formed and disrupted. **c,d,** *I-V* characteristics collected in two Pt/GO/Au nano-synapeses, showing non-volatile bipolar RS below the value of G_0, with V_{SET} ~ -4 V and V_{RESET} ~5.5 V **e,** Satistical analysis of V_{SET} and V_{RESET} for a Pt/GO/Cu nano-synapse, showing that the switching voltage when using Cu electrodes is lower than when using Au electrodes.

TOC Text

Graphene oxide (GO) is an excellent material and can be used as resistive switching medium to fabricate ultra-small (area<50 nm^2) memristive electronic synapses. Here we use a semiconductor parameter connected to the tip of a conductive atomic force microscope to prove the presence and quality of mulitple nano-synaptic behaviors. We observe that GO can be used to fabricate ultra-small and ultra-low power electronic synapses, which fit integration density requirement of industrial artificial neural networks.

Table of Contents Image

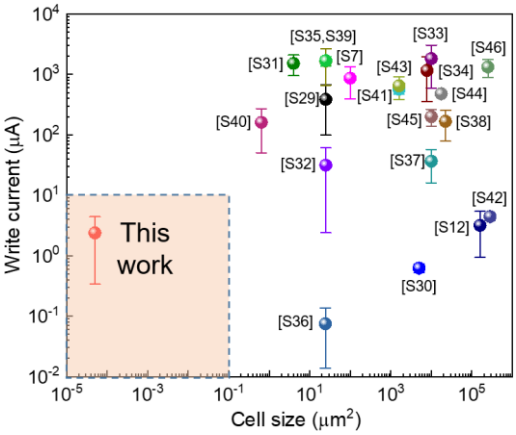

Supporting Information

Low-Power Nano-Synaptic Response in Graphene Oxide

Fei Hui, Peisong Liu, Stephen A. Hodge, Tian Carey, Chao Wen, Felice Torrisi, D. Thanuja L. Galhena, Flavia Tomarchio, Yue Lin, Enrique Moreno, Juan B. Roldan, Elad Koren, Andrea C. Ferrari, Mario Lanza**

Table S1. Summary of typical synaptic behaviors of artificial synaptic electronic devices. SLG: Single layer graphene; SM = sensory memory; LTM = long term memory; STP = short term plasticity; LTP = long term plasticity; LTD = long term depression; STDP = spike-timing dependent plasticity; SRDP = spike response dependent plasticity; PPF = paired-pulse facilitation.

Device structure	**Size**	**Tested structure**	**Synaptic functions**	**Reference**
Au/Pd/WSe_2	10 μm	Polymer electrolyte gated transistor	STP to LTP transformation	S1
Pt/InGaZnO/Pt	Ø 0.5 mm	Vertical structure	STP, LTP, Learning experience	S2
Au/SnSwe/BP/Au	5 μm	BP−SnSe heterojunction	STDP, Potentiation, depression	S3
$_{MoS2}$/hBN/SLG	~ μm	Heterostructure, Floating gate engineering	pulsed potentiation and relaxation, STDP	S4
IZO/P-doped SiO_2	80 μm	laterally coupled oxide-based protonic/electronic hybrid artificial synapse network	PPF, dynamic filtering and spatiotemporally correlated signal processing	S5
Au/Ti/MoS_2	~ μm	Biopolymer electrolyte gated MoS_2 transistor	EPSC, STDP	S6
Pt/Ag-doped SiO_xN_y/Pt	10 μm	Inert electrodes sandwiched structure	STP, LTP	S7
Ag/MgO/Pt	2 μm	Electrochemical metallization	PPD, LTP, PPF	S8
Au/Li$x$$MoS_2$/Au	5 μm	Lateral structure	Synaptic competition and synaptic cooperation effects	S9
TiN/$Ge_2Sb_2Te_5$/TiN	Ø 75 μm	T-cell phase transition area	Pair STDP	S10
Pd/Ta_2O_{5x}/TaO_y/Pd	1 μm	Crossbar structure	STDP, LTP	S11
Ni/Nb-$SrTiO_3$/Ti	Ø 400 μm	MIM structure	learning, forgetting	S12
Pt/InGaZnO/Pt	Ø 0.5 μm	Shadow mask patterned MIM	Learning experience	S13
Pt/TiO_2/Pt	2 μm	Vertical structure	Triplet-STDP, LTP	S14
HfO_x/ta/TaO_x/Pt	4 μm	MIM structure with sidewalls	Heterosynaptic interactions	S15
Au/Ti/MoS_2	5 μm	multi-terminal memristors	Cooperation/competition	S16
Pt/GO/Au	50 nm^2	CAFM tip-sample junction	Potentiation, PPF, EPSC relaxation, non-volatile RS	Our work

Table S2: Cell size of cross-point and cross-bar devices fabricated by nanolithography.

Device structure	Cell size	Fabrication technique	Reference
$Pt/TiO_2/Pt$	50 nm×50 nm	nanoimprint lithography	S17
$TiN/Hf/HfO_x/TiN$	10 nm×10 nm	E-beam lithography	S18
Pt/Cr/Ag-Si/Si/W	100 nm×100 nm	E-beam lithography	S19
Pt/GO/Au, Pt/GO/Cu	50 nm^2	-	Our work

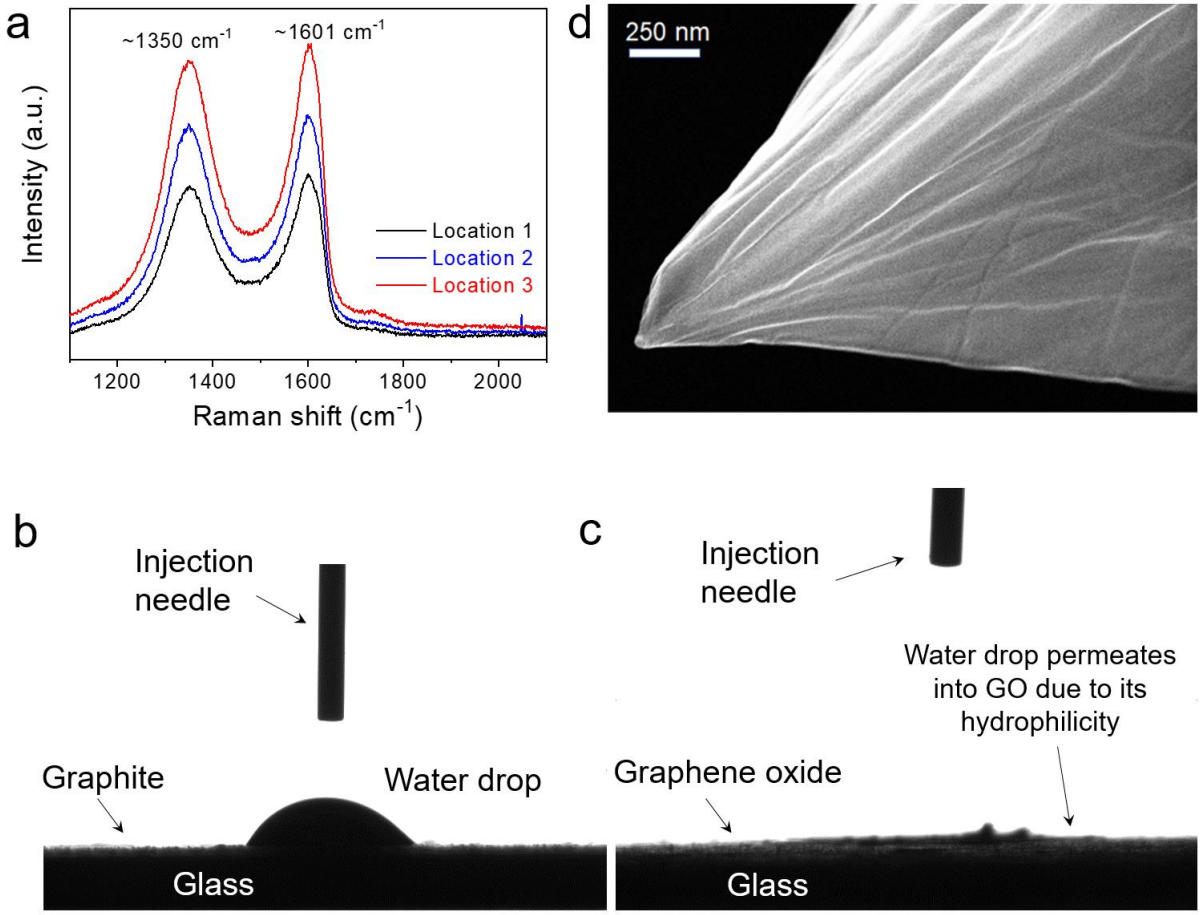

Supplementary Figure 1: (a) Raman spectra of graphene oxide on different locations. (b) and (c) Wettability measurement of graphite and graphene oxide (GO), respectively. GO exhibits good hydrophilic properties, indicating the exisit of large amount of oxygen-containing functional groups. (d) SEM image of CAFM tip (Type: Arrow CONTPt) after spray-coating with a ~100 nm thick GO film. The image shows conformal coating. GO is recognized by the formation of wrinkles.

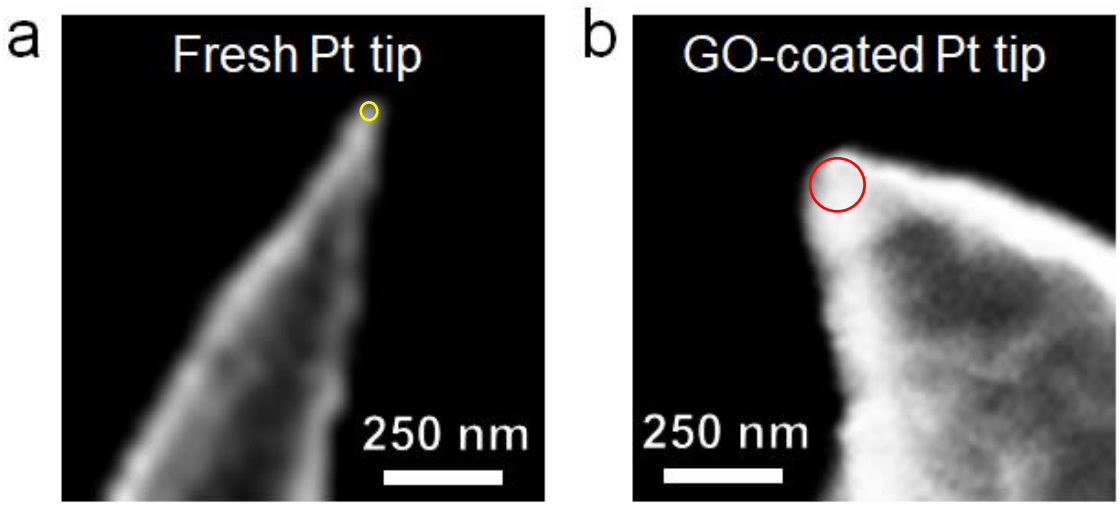

Supplementary Figure 2: Zoomed-in images of (a) fresh Pt tip (b) GO-coated Pt tip cropped from the SEM images in Figures 1c, d of the main text, respectively. The radius of each tip (highlighted with a yellow and red circles) can be estimated to be ~8 nm (fresh tip) and ~65 nm (GO-coated).

Supplementary Note 1: Effective contact area between tip and sample

According to Hertz contact theory [S20-S21], the most used to study interactions between tip and sample in AFM systems [S20-S23], A_c can be quantified as [S20-S21]:

$$A_c = \pi \cdot {r_c}^2 = \pi \left(\frac{F_c R_{tip}}{K}\right)^{2/3} \quad \text{with } \frac{1}{K} = \frac{3}{4}\left(\frac{1-v_1^2}{E_1} + \frac{1-v_2^2}{E_2}\right) \qquad \text{(Eq.S1)}$$

where r_c is the contact radius (the radius of the contact area), F_c is the contact force between tip and sample, R_{tip} is the tip radius, $E_{1/2}$ are the elasticity moduli and $v_{1/2}$ are the Poisson ratios of tip and sample. F_c is given by the Hooke's law [S24]:

$$F_c = -k_c \cdot \delta_c + F_{ext} \qquad \text{(Eq. S2)}$$

where k_c is the spring constant of the tip, δ_c is the tip deflection, and F_{ext} is the sum of external forces, such as capillary forces, electrostatic forces and others [S25].

Ref.S26 reported calculations of the value of A_C for different R_{tip}, F_C, and tip/sample materials composition, giving a 1-1000 nm^2 range [S26]. However, the effective area (A_{eff}), defined as the sum of all the spatial locations on the surface of the sample electrically connected to the CAFM, across which the electrons can flow, also depends on relative humidity [S26], and the thickness of the water layer on the surface of tip and sample [S27]. Therefore, when studying insulating materials with a CAFM tip in air, A_{eff} is normally>A_C [S26]. We estimate the tip/sample contact area, i.e. the size of the Pt/GO/Au nano-synapses (formed by placing a Pt tip on GO/Au sample) and Pt/GO/Cu nano-synapses (formed by placing a Pt/GO tip on a Cu surface) is very small (<50 nm^2) [S27].

Ref.S27 reported that the most (statistically) accepted value for A_{eff} when using sharp Pt tips (R_{tip} <25 nm) on the surface of SiO_2 is ~50 nm^2. This tip/sample system is similar to our Pt/GO/Au nano-synapses, with the only difference that our Pt tip is sharper (R_{tip} ~8 nm, see Supplementary Fig.2a) and that the GO film is softer than Pt. According to Eq.1, a smaller R_{tip} decreases A_{eff}, and softer materials increase A_{eff}. For this reason, in our experiments we use a very low deflection setpoint (i.e. F_C) ~0.2 V, to minimize tip penetration into the GO film. There is no tip penetration into GO because topographic

AFM maps collected after tip landing on the GO surface do not show any hole. Therefore, the size of our Pt/GO/Au nano-synapses is slightly <50 nm^2.

When GO-coated Pt tips are placed in contact with the Cu surface in order to form Pt/GO/Cu nano-synapses, the radius of the GO-coated Pt tip is ~65 nm, Fig. S2b. Refs. S27-S28 reported that an increase of R_{tip} by~20 times produces a one order of magnitude increase of A_C (from Eq. S1 this would be $20^{2/3}$ = 7.36). Therefore, as the radius of the GO-coated Pt tip is ~65 nm (i.e. ~8 times larger than that the~8nm size of the of Pt tip), the size of the Pt/GO/Cu nano-synapse (i.e. the tip/sample contact area) is not >500 nm^2.

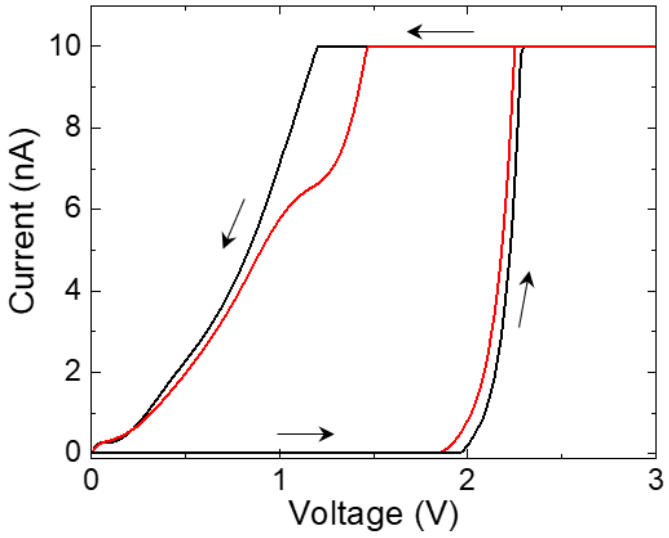

Supplementary Figure 3: *I-V* curves showing volatile resistive switching characteristics in Pt/GO/Au synapses. Each *I-V* curve (read and black) correspond to different positions.

Table S3: Write current of memristive synapses with different device sizes.

Synapse structure	Device size (μm^2)	Write voltage (V)	Write current / power 1st pulse	Write current/ power last pulse	# pulses	Ref.
Au/hBN/Au	25	5.8	70 μA / 406 μW	760 μA / 4.4 mW	26	S29
Ag/CH3NH3PbI3-*x*Cl*x*/FTO	5000	0.5	0.5 μA / 0.25 μW	0.75 μA / 0.38 μW	10	S30
Pt/SiO_xN_y:Ag/Pt	100	2.8	250 μA / 700 μW	1400 μA / 3.9 mW	500	S7
TiN/TaO_x/Pt	4	1	800 μA / 800 μW	2200 μA / 2.2 mW	300	S31
Ni/Nb-$SrTiO_3$/Ti	160000	6	0.5 μA / 3 μW	6 μA / 36 μW	62	S12
Au/Ti/h-BN/Cu	25	0.7	1 μA / 0.7 μW	70 μA / 49 μW	19	S32
Ag/$Zr_{0.5}Hf_{0.5}O_2$:GOQDs/Ag	10000	0.8	200 μA / 160 μW	3000 μA / 2.4 mW	30	S33
Ag/N-GOQDs/Pt	7850	0.3	100 μA / 30 μW	2000 μA / 600 μW	30	S34
Cu/pV_3D_3/AI	25	2 ~4	750 μA / 2.3 mW	3000 μA / 9 mW	50	S35
Au/WS_2/PZT/Au	24.3	3.5	0 μA / 0 μW	0.15 μA / 0.53 μW	10	S36
Ag/CιC:Ag/ITO	10000	0.8~1.1	10 μA / 10 μW	60 μA / 60 μW	100	S37
ITO/ZnO/ITO	22500	1	50 μA / 50 μW	250 μA / 250 μW	150	S38
W/Ag/MgO/Ag/W	25	3	1300 μA / 4 mW	2000 μA / 6 mW	10	S39
Pt/LSO/TiN/Ti/SiO_2/Si	0.64	0.1	30 μA / 0.3 μW	300 μA / 30 μW	100	S40
TiN/HfO_2/Ti/TiN	1600	0.7	460 μA / 322 μW	700 μA / 490 μW	300	S41
Pt/WOx/Ti	282600	2	3.6 μA / 7.2 μW	5.2 μA / 10.4 μW	50	S42
TiN /HfO_2/Pt	1600	1	400 μA / 400 μW	1000 μA / 1 mW	300	S43
Pt/HfOx/ZnOx/TiN	17662	2	420 μA / 840 μW	540 μA / 1 mW	80	S44
ITO/LiF/CuPc/Al	10000	11	120 μA / 1.3 mW	270 μA / 3 mW	10	S45
Au/C_3N/PVPy/ITO	250000	5	750 μA / 3.8 mW	1800 μA / 9 mW	14	S46
Pt/GO/Au	5×10^{-5}	3	0.03 μA / 0.1 μW	5 μA / 15 μW	50	This work

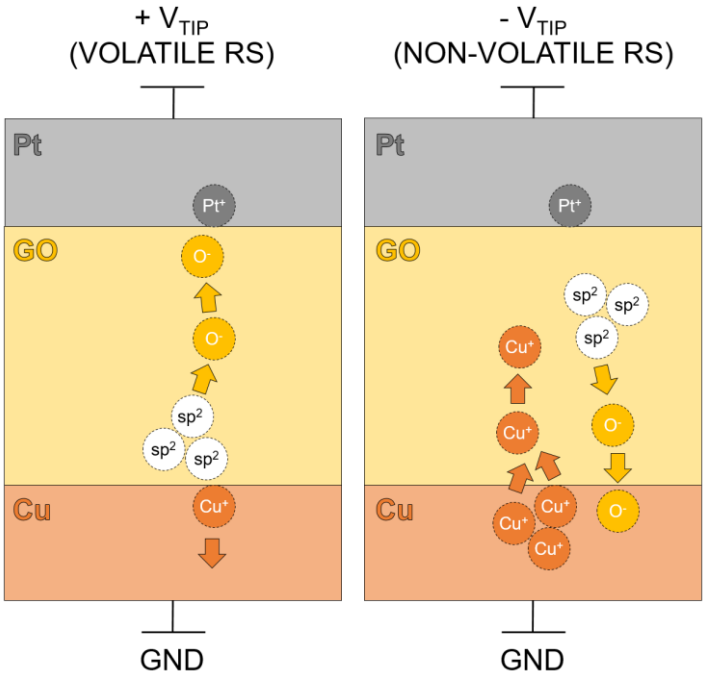

Supplementary Figure 4: Schematic displaying the switching mechanism in volatile regime (left) and non-volatile regime (right). The migration of oxygen requires low energy and, at the low current levels (<1 μA) presented in that regime, these defects are volatile. The migration of Cu^+ (or Au^+) ions produces non-volatile conductance changes because they are heavier and cannot recover their initial state when the bias is switched off.

Supplementary Note 2: Thermal simulations

We simulate the current across the Pt/GO/Au nano-synapse in LRS before the reset event, using the model developed in Ref. [S51], and comparing the resulting values with experiments. We estimate the resistance of the Pt/GO/Au nano-synapse and solve the three-dimensional heat equation [Eq. S5]. The simulation is designed taking into consideration that the thickness of the GO film is ~50 nm. The top Pt electrode has the shape of a CAFM tip, and the bottom electrode consists of a Au layer.

The 3D heat equation (3DHE) in Eq.S5 is solved using a fully explicit finite difference method [S50]. Therefore, the features of the nano-synapses that are thermally dependent are correctly described. The grid consists of 301 × 301 × 751 nodes, with a uniform mesh with 0.2 nm grid mesh distance (in line with comparable simulations [S51-S52]). Dirichlet boundary conditions [S53] are employed at the outer electrode layer surfaces, and room temperature is assumed outside the device (due to the high electrode thermal conductivity (Au: 317 W/mK, Pt: 71.6 W/mK) [S54]). Perfectly matched layers (PML) are used at the lateral faces [S51, S55-S56] to describe open boundary problems, such as ours.

$$\dot{q} = -\nabla[k_{th}(x,y,z)\nabla T(x,y,z)] \quad \text{(Eq. S5)}$$

We account for Joule heating to determine the heat generation rate ($\dot{q}$) in Eq.S5. As the current is generated by applying negative bias to the CAFM tip, it is expected to consist of Au^+ ions that migrate from the Au bottom electrode towards the cathode (Pt tip). A non-fully formed conductive path is assumed with a high electrical conductance and truncated-cone shaped [S57-S58]. The temperature peak is achieved at the narrower part of this region, see Figure S5. The heat generation rate ($\dot{q}$) is calculated using the electrical conductivity and the electric field distribution in the Pt/GO/Au nano-synapse.

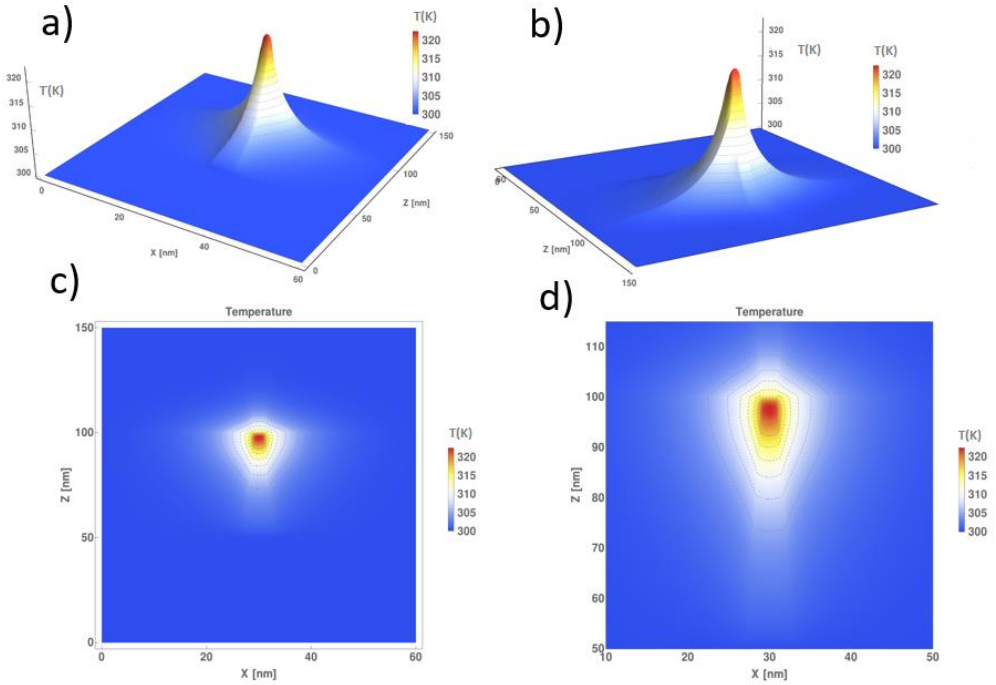

Figure S5: Three-dimensional temperature distribution for different cross-sections in the device structure (Fig. 1 in the main text). The simulations are performed for 6V in the LRS, the simulated current is equal to the experimental one for one of the cycles in Fig. 4c in the main text (30 μA). (a) Longitudinal cross-section in the XZ plane (the non-continuous conductive path extends from Z=50 to 100nm), taken in the middle of the simulation domain. The variations in the temperature distribution correspond to the limited extension of the AFM tip, affecting the final result. (b) Same cross-section as (a) from another bird's eye view. (c,d) contour plots of the temperature distributions in (a,b), respectively.

For the electrodes, 3D thermal conductivity values are employed K_{TH} (Au) = 317 W/Km [S54], K_{TH} (Pt) =71.6 W/Km [S54]. The partially formed conductive path is assumed to have a thermal conductivity [K_{TH} (path)~15 W/Km], which is consistent with that of Refs. [S52, S59]. For GO we use K_{TH} (GO)~2.83 W/Km [S60]. The weighted residual method is employed to numerically solve the heat equation [S51, S61].

Table S4: Physical parameters used in the simulations [S51,S52,S54,S59,S60,S61]

K_{TH} (Au)	317 W K^{-1} m^{-1}	Cu thermal conductivity
K_{TH} (path)	15 W K^{-1} m^{-1}	Conductive path thermal conductivity
K_{TH} (Pt)	71.6 W K^{-1} m^{-1}	Pt thermal conductivity
K_{TH} (GO)	2.83 W K^{-1} m^{-1}	GO thermal conductivity
σ_{CF_path}	1.67 x 10^6 Ω^{-1} m^{-1}	Conductive path conductivity
T_0	300 K	Room temperature

A simulation is performed, using current and voltage data corresponding to the *I-V* curves measured in Fig. 4c in the main text, with the parameters in Table S5. The thermally activated physical mechanisms behind RS trigger the broadening of the gaps in the conductive path that gives the reset process (see Fig.4c in the main text). Therefore, the thermal description is crucial for the study of our Pt/GO/Au nano-synapses [S56-S57].

References

[S1] Zhu, J. *et al.* Ion gated synaptic transistors based on 2D van der Waals crystals with tunable diffusive dynamics *Adv. Mater.* **30**, 1800195 (2018).

[S2] Wang, Z. Q. *et al.* Synaptic Learning and Memory Functions Achieved Using Oxygen Ion Migration/Diffusion in an Amorphous InGaZnO Memristor. *Adv. Funct. Mater.* **22**, 2759 (2012).

[S3] Tian, H. *et al.* Emulating Bilingual Synaptic Response Using a Junction-Based Artificial Synaptic Device. *ACS Nano* **11**, 7156 (2017).

[S4] Paul, T., Ahmed, T., Kanhaiya Tiwari, K., Singh Thakur, C., Ghosh, A. A high-performance MoS2 synaptic device with floating gate engineering for neuromorphic computing. *2D Mater.* **6**, 045008 (2019).

[S5] Zhu, L. Q., Wan, C. J., Guo, L. Q., Shi, Y., Wan, Q. Artificial synapse network on inorganic proton conductor for neuromorphic systems. *Nat. Commun.* **5**, 3158 (2014).

[S6] Jiang, J. *et al.* 2D electric-double-layer phototransistor for photoelectronic and spatiotemporal hybrid neuromorphic integration. *Nanoscale* **11**, 1360 (2019).

[S7] Wang, Z. *et al.* Memristors with diffusive dynamics as synaptic emulators for neuromorphic computing. *Nat. Mater.* **16**, 101–108 (2017).

[S8] Zhang, Y., Zhong, S., Song, L., Ji, X., Zhao, R. Emulating dynamic synaptic plasticity over broad timescales with memristive device. *Appl. Phys. Lett.* **113**, 203102 (2018).

[S9] Zhu, X., Li, D., Liang, X., Lu, W. D. Ionic modulation and ionic coupling effects in MoS2 devices for neuromorphic computing. *Nat. Mater.* **18**, 141 (2019).

[S10] Kuzum, D., Jeyasingh, R. G. D., Lee, B., Wong, H.S.P. Nanoelectronic Programmable Synapses Based on Phase Change Materials for Brain-Inspired Computing. *Nano Lett.* **12**, 2179-2186 (2012).

[S11] Kim, S. *et al.* Experimental Demonstration of a Second-Order Memristor and Its Ability to Biorealistically Implement Synaptic Plasticity. *Nano Lett.* **15**, 2203−2211 (2015).

[S12] Yin, X. B. et al. Mimicking the brain functions of learning, forgetting and explicit/implicit memories with SrTiO3-based memristive devices. *Phys. Chem. Chem. Phys.*, **18**, 31796-31802 (2016).

[S13] Wang, Z. Q. et al. Synaptic Learning and Memory Functions Achieved Using Oxygen Ion Migration/Diffusion in an Amorphous InGaZnO Memristor. *Adv. Funct. Mater.* **22**, 2759–2765 (2012).

[S14] Wei, S. L. et al. Emulating long-term synaptic dynamics with memristive devices. arXiv:1509.01998.

[S15] Yang, Y. et al. Multifunctional nanoionic devices enabling simultaneous heterosynaptic plasticity and efficient in-memory boolean logic. *Adv. Electron. Mater.* **3**, 1700032 (2017).

[S16] Sangwan, V. K. et al. Multi-terminal memtransistors from polycrystalline monolayer molybdenum disulfide. *Nature* **554**, 500 (2018).

[S17] J. J. Yang, et al. Memristive switching mechanism for metal/oxide/metal nanodevices. *Nat. Nanotechnol.* **3**, 429 (2008).

[S18] B. Govoreanu et al. 10x10 nm^2 Hf/HfO_x crossbar resistive RAM with excellent performance, reliability and low-energy operation. *IEEE IEDM* DOI: 10.1109/IEDM.2011.6131652 (2011).

[S19] S. H. Jo, et al. Nanoscale memristor device as synapse in neuromorphic systems. *Nano Lett.* **10**, 1297-1301 (2010).

[S20] Olbrich, A. "Characterisation of thin dielectrics by means of modified atomic force microscopy", PhD thesis, University of Regensburg, Regensburg, Germany (1999).

[S21] B. Bhushan (Ed.), Springer Handbook of Nanotechnology, Springer-Verlag, Berlin (2004).

[S22] Ruskell, T. G. *et al.* Novel millimeter-wave near-field resistivity microscope. *Appl. Phys. Lett.* **68**, 9 (1996).

[S23] A. Born, "Applications of scanning capacitance microscopy and scanning probe microscopy techniques in nanotechnology", PhD thesis, University of Hamburg, Germany,

http://www.physnet.unihamburg.de/services/fachinfo/_Volltexte/Axel_Born/Axel_Bron.htm (accessed on January 18, 2015).

[S24] Louey, M. D.; Mulvaney, P.; Stewart, P. J. *J. Pharm. Biomed. Anal.* **29**, 559 (2001).

[S25] Cappella, B.; Dietler, G. Force-distance curves by atomic force microscopy. *Surf. Sci. Rep.* **34**, 1 (1999).

[S26] Pan, C., Shi., Y., Hui, F., Grustan-Gutierrez, E. & Lanza, M. in Conductive Atomic Force Microscopy: Application in Nanomaterials (ed. Lanza, M.) Ch. 1 (Wiley-VCH, 2017).

[S27] Frammeblsberger, W., Benstetter, G., Kiely, J., Stamp, R. C-AFM-based thickness determination of thin and ultra-thin SiO2 films by use of different conductive-coated probe tips. *Appl. Surf. Sci.* **253**, 3615-3626 (2007).

[S28] Frammelsberger, W., Benstetter, G., Kiely, J., Stamp, R. Thickness determination of thin and ultra-thin SiO2 films by C-AFM IV-spectroscopy. *Appl. Surf. Sci.* **252**, 2375 (2006).

[S29] Chen, S. C. *et al.* Wafer-scale integration of 2D materials in high-density memristive crossbar arrays for artificial neural networks. *Nat. Electron*. 3, 638-645 (2020).

[S30] Yoo, E. *et al.* Bifunctional resistive switching behavior in an organolead halide perovskite based Ag/$CH_3NH_3PbI_{3-x}Cl_x$/FTO structure. *J. Mater. Chem. C* 7824-7830 (2016).

[S31] Wang, Z. W. *et al.* Engineering incremental resistive switching in TaOx based memristors for brain-inspired computing. *Nanoscale* **8**, 14015-14022 (2016).

[S32] Xiao, M. One-dimensional Titanium Dioxide Nanomaterial based Memristive Device and its Neuromorphic Computing Applications, PhD thesis, *UWSpace*. http://hdl.handle.net/10012/14872 (2019).

[S33] Yan, X. B. *et al.* Graphene Oxide Quantum Dots Based Memristors with Progressive Conduction Tuning for Artificial Synaptic Learning. *Adv. Funct. Mater.* 1803728 (2018).

[S34] Sokolov, A.S. *et al.* Silver-Adapted Diffusive Memristor Based on Organic Nitrogen-Doped Graphene Oxide Quantum Dots (N-GOQDs) for Artificial Biosynapse Applications. *Adv. Funct. Mater*. **29**, 1807504 (2019).

[S35] Jiang, B. C. *et al.* Polymer analog memristive synapse with atomic-scale conductive filament for flexible neuromorphic computing system *Nano Lett*. **19**, 839−849 (2019).

[S36] Luo, Z-. D. *et al.* Artificial Optoelectronic Synapses Based on Ferroelectric Field-Effect Enabled 2D Transition Metal Dichalcogenide Memristive Transistors. *ACS Nano* **14**, 746–754 (2020).

[S37] Ge, J. *et al.* Memristive synapses with high reproducibility for flexible neuromorphic networks based on biological nanocomposites. *Nanoscale*, **12**, 720-730 (2020).

[S38] Chandrasekaran, S., Simanjuntak, F. M., Panda, D., Tseng, T.-Y. Enhanced Synaptic Linearity in ZnO-Based Invisible Memristive Synapse by Introducing Double Pulsing Scheme. *IEEE Transactions on Electron Devices* **66**, 4722-4726 (2019).

[S39] Sun, J. *et al.* Physically Transient Memristive Synapse With Short-Term Plasticity Based on Magnesium Oxide. *IEEE Electron Device Letters* **40**, 706-709 (2019).

[S40] Chen, J. *et al.* LiSiOX-Based Analog Memristive Synapse for Neuromorphic Computing. IEEE Electron Device Letters **40**, 542-545 (2019).

[S41] Covi, E. *et al.* Analog Memristive Synapse in Spiking Networks Implementing Unsupervised Learning. *Front. Neurosci.* **10**, 482 (2016).

[S42] Lin, Y. *et al.* Transferable and Flexible Artificial Memristive Synapse Based on WOx Schottky Junction on Arbitrary Substrates. *Adv. Funct. Mater*. **4**, 1800373 (2018).

[S43] Covi. E. *et al*. Spike-driven threshold-based learning with memristive synapses and neuromorphic silicon neurons. *J. Phys. D: Appl. Phys.* **51** 344003 (2018).

[S44] Wang, L. G. *et al*. Synaptic Plasticity and Learning Behaviors Mimicked in Single Inorganic Synapses of Pt/HfOx/ZnOx/TiN Memristive System. *Nanoscale Research Letters* **12**, 65 (2017).

[S45] Wang, L. *et al.* Rectification-Regulated Memristive Characteristics in Electron-Type CuPc-Based Element for Electrical Synapse. *Adv. Electron. Mater*. 3, 1700063 (2017).

[S46] Zhou, L. *et al.* Tunable synaptic behavior realized in C_3N composite based memristor. *Nano Energy* **58**, 293-303 (2019).

[S47] Pan, C. *et al.* Model for multi-filamentary conduction in graphene/hexagonal-boron-nitride/graphene based resistive switching devices. *2D Mater.* **4**, 025099 (2017).
[S48] Roldán, J. B. *et al.* Multivariate analysis and extraction of parameters in resistive RAMs using the Quantum Point Contact model. *J. Appl. Phys.* **123**, 014501 (2018).
[S49] Lee, D. *et al.* Quantum confinement-induced tunable exciton states in graphene oxide. *Sci. Rep.* **3**, 2250 (2013).
[S50] Mazumder, S. Numerical methods for partial differential equations : finite difference and finite volume methods, Academic Press, 2015.
[S51] Maestro, M. *et al.* Unipolar resistive switching behavior in Al_2O_3/HfO_2 multilayer dielectric stacks: fabrication, characterization and simulation. *Nanotechnology* **31**, 135202 (2020).
[S52] Aldana, S. et al. A 3D kinetic Monte Carlo simulation study of resistive switching processes in Ni/HfO2/Si-n+-based RRAMs. J. Phys. D: Appl. Phys. 50, (2017).
[S53] Cheng, A., D., Cheng T. Heritage and early history of the boundary element method, *Engineering Analysis with Boundary Elements*, **29**, 268–302 (2005).
[S54] https://www.engineeringtoolbox.com/thermal-conductivity-metals-d_858.html
[S55] Lantos, N., Nataf, F. Perfectly matched layers for the heat and advection–diffusion equations, *J. Comput. Phys*. **229**, 9042–9052 (2010).
[S56] Moreno, E. *et al.* Implementation of Open Boundary Problems in Photo-Conductive Antennas by Using Convolutional Perfectly Matched Layers. *IEEE Trans. Antennas Propag.* **64**, 4919–4922 (2016).
[S57] Aldana, S. *et al.* An in-depth description of bipolar resistive switching in Cu/HfOx/Pt devices, a 3D Kinetic Monte Carlo simulation approach. *J. Appl. Phys.* **123**, 154501 (2018).
[S58] Rodriguez, N. *et al.* Resistive switching and charge transport in laser-fabricated graphene oxide memristors: a Time Series and Quantum Point Contact modelling approach. *Materials* **12**, 3734 (2019).
[S59] Ielmini, D. Modeling the universal set/reset characteristics of bipolar RRAM by field- and temperature-driven filament growth. *IEEE Trans. Electron Devices.* **58**, 4309-4317 (2011).
[S60] Zeng W. *et al*. Defect-engineered reduced graphene oxide sheets with high electric conductivity and controlled thermal conductivity for soft and flexible wearable thermoelectric generators. *Nano Energy* **54**, 163-174 (2018).
[S61] B.A. Finlayson, The method of weighted residuals and variational principles: with application in fluid mechanics, heat and mass transfer, Academic Press, (1972).